Static and Dynamic Elastic Properties of Fractal-cut Materials

Valentin Kunin[1,2], Shu Yang[1], Yigil Cho[1], Pierre Deymier[4], David J. Srolovitz[1,3]
[1]*Department of Materials Science and Engineering,*
[2]*Department of Applied Mathematics and Computational Science,*
[3]*Department of Mechanical Engineering and Applied Mechanics,*
University of Pennsylvania, Philadelphia, PA 19104, USA,
[4]*Department of Materials Science and Engineering,*
The University of Arizona, Tucson, AZ 85721 USA

We investigate the static and dynamic (phononic) elastic behavior of fractal-cut materials. These materials are novel in the sense that they deform by rotation of "rigid" units rather than by straining these units, can be fabricated by exploiting a simple cutting paradigm, and have properties that can be manipulated by control of the cut pattern and its hierarchy. We show that variation of fractal-cut level and cut pattern can be exploited to manipulate the symmetry of the elastic constant tensor, the elastic limit of deformation, and, therefore, the elastic response. By studying phonon behavior, we demonstrate how some cut symmetries naturally open acoustic band gaps. Several of the important features of the band structure can be directly related to the static elastic properties. Based upon our phonon calculations, we predict the acoustic transmission spectrum of an example fractal-cut structure and validated it through 3D printing and sound attenuation experiments.

Keywords. Phononic crystals; Acoustic band gaps; Auxetics; Tunable elastic properties.

INTRODUCTION

Heterogeneity in the structure of materials occurs commonly in natural materials and can be exploited in engineering materials to produce combinations of properties tailored for particular classes of applications. In most cases, the distributions of phases within materials exhibits a substantial degree of randomness. Exceptions include such engineered composites as laminates, aligned fiber composites, and woven structures. For many applications, it is desirable for the phases to have properties from opposite extremes; e.g., strong/brittle phases and weak/ductile phases. Other examples include cases where the elastic constants are either large or zero (i.e., holes). In this report, we consider the elastic (static and dynamic) properties of a uniform 2D material into which we introduce a periodic, hierarchical array of cuts; we refer to these as fractal-cut materials [1, 2]. Such materials can be designed to produce a wide range of interesting and useful properties.

Consider the case of a square sheet with horizontal and vertical cuts. In the example shown in Fig. 1a, a horizontal cut is made nearly across the sample leaving a ligament at the left and right edges and vertical cuts are made from the top and bottom surface to just short of the center, leaving ligaments at the center. When this structure is subject to nearly any external loading, it opens by rotation of section relative to other at the ligaments/hinges (Fig. 1a). In the limit that the ligament size goes to zero, the sections of the material between cuts remain undeformed during the rotation.Hence, we idealize this material as a set of rigid bodies, connected by hinges (in 2D or 3D) or possibly universal joints (in 3D). This process of separating the material into rotating blocks can be repeated in a hierarchical form by cutting the previously rigid/rotatable blocks. If this is done *ad infinitum*, the resultant structure is a fractal (see Fig. 1). Such structures have novel mechanical and dynamical properties associated with these two central features; rotatable units and structure across a range of scales.

Simple rotatable structures [3] can produce materials with negative Poisson ratios (i.e., auxetics) [4–6]; fractal-cut geometries can give rise to extremely large dilatations [1, 2]. Such rotations are central to the auxetic behavior of several perovskite structures [7]. One natural consequence of the extremely large dilatations achievable with fractal-cut sheets is their ability to wrap non-zero Gauss curvature objects without wrinkling or tearing even when the matrix material is elastically rigid [1].

In addition to interesting elastic/geometric properties, fractal-cut materials also exhibit interesting dynamic (phononic) properties. Since our fractal-cut materials are periodic, there is a possibility that such structures may exhibit band gaps in the phonon spectrum (i.e., frequency ranges in which sound does not propagate); such periodic metamaterials are known as phononic crystals. The phononic band structure is dictated by the acoustic properties of the constituent materials and their spatial distribution (in the present case, one phase is solid and the other is air/vacuum). Unit cell geometries that have been exploited in the design of phononic crystals vary from very simple [8] to complex [9], including fractals [10–12].

The most obvious application of phononic crystals is in sound insulation (e.g., [13]); however, the high cost of manufacturing such periodic structures makes most such applications untenable. However, acoustic metamaterials have a number of other interesting applications including waveguides [14] in which sound can be channeled into different directions with little energy loss, phononic lenses

[15] akin to optical lenses, and devices which exploit negative refraction [16].

One important challenge in acoustic applications is to design metamaterials such that the band gaps fall into the frequency range of interest. For acoustic applications, this is below 1 kHz. However, since vibrational frequencies scale inversely with unit cell size; 1 kHz commonly implies meter length scales. Such scales are usually impractical; hence, an important challenge is to design materials with wide, low frequency band gaps and of reasonable size. While recent advances based upon resonant structures have pushed band gaps into the desired low frequency region [17], the resultant band gaps are too narrow for many applications. Since fractal-cut materials can be designed with tunable elastic properties, we investigate here how such materials can be designed to manipulate acoustic properties. As we demonstrate below, elastic properties can be used as a simple predictor of several important features of the dynamical response of these materials.

In this paper, we report how the elastic (static and dynamic) properties of such rotatable, fractal-cut structures vary with degree of hierarchy, cut-pattern symmetry, and hinge properties. We begin with an analysis of the geometric properties of rotatable hinge, fractal-cut structures and then analyze the impact of finite hinge stiffness in order to predict the elastic behavior (elastic constants) of such structures. Since real fractal-cut materials will always have finite ligament sizes, we perform finite element analyses in order to determine the correlation between hinge stiffness and ligament geometries in elastic materials (where both the ligament and blocks are made from the same material). Next, we consider dynamic elastic properties by analyzing sound propagation through these materials - determining the phonon band structure.We then exploit 3D printing to manufacture a fractal-like structure and measure its acoustic properties to compare with our predictions. Finally, we examine the correlation between the static and dynamic elastic results in order to provide guidance for the design of such materials.

STATIC ELASTIC PROPERTIES

In this paper, we consider square and hexagonal unit cell structures repeated to produce (square and Kagome [18–20]) lattices [1]. We first focus on square lattices. Consider splitting a square into four smaller squares, connected by hinges (Fig. 1a) to form a "level 1 square lattice" (Fig. 1d). If the squares are perfectly rigid and the hinges are of zero size, this structure has only one degree of freedom (i.e. the angle between two adjacent squares describes the entire lattice). If the lattice is elongated in any (for example, horizontal) direction, the strain in the orthogonal (vertical here) direction is identical; i.e., the Poisson ratio is $\nu = -1$ (it is ideally auxetic).

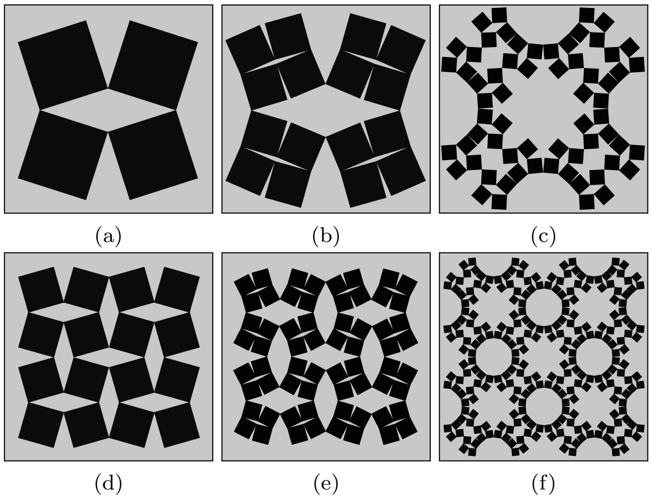

FIG. 1. Example of a (a) "square unit cell" that can be (d) repeated to create a "square lattice"; a level 1 structure. Each square can be subsequently divided in exactly the same manner to create a (b) level 2 structure which may be (e) repeated to form a level 2 lattice. (c) and (f) show the corresponding level 3 structures/lattices.

Each small square in the original, level 1, structure, can be cut into four even smaller squares in exactly the same manner , producing a level 2 square unit cell (Fig. 1b) which may be repeated to form an infinite periodic level 2 lattice (Fig. 1e). The procedure of cutting each square into four sub-squares connected by hinges may be repeated n times to create a level n structures (see Fig. 1). In the limit that $n \to \infty$, such a structure is a fractal. The same approach can be applied to the hexagonal/Kagome [18] case, as shown in Fig. 2. For both lattice, the level 1 structures have only one degree of freedom and a Poisson ratio of -1. As the level of the structures increase, the open structures become less dense/more tenuous and have large holes.

The ideal case - free-hinges, rigid bodies

We focus first on the ideal case, where the fundamental geometrical units (squares or triangles) are perfectly rigid and the hinges are of zero size and rotate freely. The level 1 square structure is particularly simple; it has only one degree of freedom, the angle β (see Fig. 3a). To avoid overlapping units $0 \le \beta \le \pi/2$. This implies that the strains $\varepsilon_{xx} = \varepsilon_{yy}$. These strains are

$$\varepsilon_{xx} = \varepsilon_{yy} = \sin\beta + \cos\beta - 1; \qquad \varepsilon_{xy} = 0. \tag{1}$$

Note that unlike homogeneous (uncut) materials the structure is not a unique function of strain; β and $\pi/2 - \beta$ generate exactly same strains albeit with different lat-

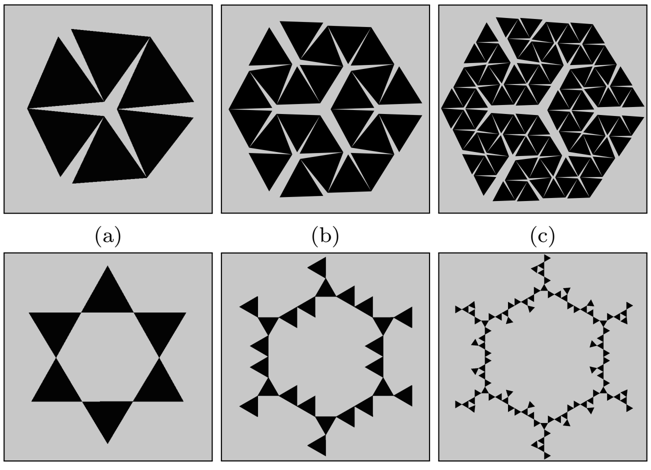
(a) (b) (c)

(d) (e) (f)

FIG. 2. Examples of (a) level 1, (b) level 2, and (c) level 3 Kagome unit cells that are nearly closed. (d), (e) and (f) show the corresponding fully stretched structures (scaled to fit in the same size boxes) for which the strains are $\epsilon^* = 1$, $\sqrt{3} = 1.71$, and $2\sqrt{3} - 1/2 = 2.96$, respectively.

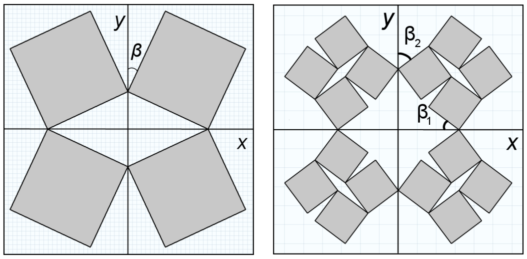

(a) (b)

FIG. 3. Suggested parameterization of the (a) level 1 and (b) level 2 square lattice.

tice geometries/states. Possible geometrical states of level 2 include those of level 1, but because level 2 has two degrees of freedom (we parameterize as (β_1, β_2) $0 \le \beta_1 \le \beta_2 \le \pi/2$ in Fig. 3b) many more states are available. The corresponding strains are

$$\begin{aligned} \varepsilon_{xx}(\beta_1, \beta_2) &= \sin\beta_2 + \frac{1}{2}(\cos\beta_1 + \cos\beta_2) - 1 \\ \varepsilon_{yy}(\beta_1, \beta_2) &= \cos\beta_1 + \frac{1}{2}(\sin\beta_1 + \sin\beta_2) - 1 \\ \varepsilon_{xy} &= 0. \end{aligned} \tag{2}$$

Some strains may be generated by only one state (set of βs) but, like for level 1, some may be generated by two different states. Figure 4 shows the accessible strains for the level 2 square lattice as well as the number of states that can access each strain. Several states labeled in Fig. 4 are shown explicitly in Fig. 5; these states are special in the following sense. "A" corresponds to the maximum dilatation of level 1. There are two states which generate the strain "B"; the one shown in Fig. 5b is stable and incompressible while the other, shown in Fig. 5c, is only special in the sense that it corresponds to the same strain as Fig. 5b. "C" corresponds to the maximum uniaxial strain (in the x-direction).

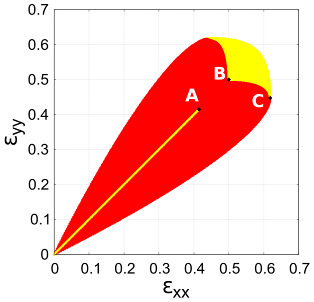

FIG. 4. Accessible strains of the level 2 square lattice; white indicates inaccessible strain states, red indicates strains for which only one state exists and yellow indicates strains which may be realized in two ways (sets of βs). Points A ($\varepsilon_{xx} = \varepsilon_{yy} = \sqrt{2} - 1$), B ($\varepsilon_{xx} = \varepsilon_{yy} = 1/2$), and C ($\varepsilon_{xx} = (\sqrt{5} - 1)/2$, $\varepsilon_{yy} = 1/\sqrt{5}$) are special and correspond to the structures shown in Fig. 5.

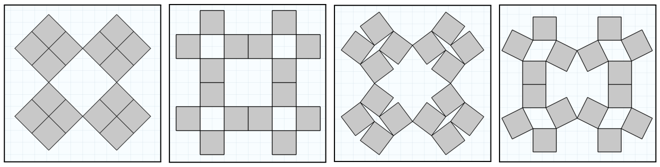
(a) (b) (c) (d)

FIG. 5. Special states of the level 2 square lattice (see Fig. 4). (a) generates strain A, (b) and (c) both generate strain B and (d) generates state C.

What is the total number of degrees of freedom of a level n lattice? It may be estimated as follows. The unit cell of a level n periodic lattice consists of $N_\square(n) = 4^n$ squares with $N_h(n) = (4^{n+1} + 8)/3$ hinges per unit cell. Since each square has three degrees of freedom (two translations and one rotation) and each hinge constrains two of these, the total number of degrees of freedom is

$$N_{DOF}(n) = 3N_\square(n) - 2N_h(n) = \frac{4^n - 16}{3}, \tag{3}$$

where the last expression is applicable at large n. This formula does not account for linearly dependent degrees of freedom. The linearly dependent degrees of freedom tend to zero as $n \to \infty$; hence Eq. 3 should be viewed as asymptotic for large n and as approximate at smaller n. Clearly, this is a very poor approximation for $n = 1$ (1-exact, -4-estimate), $n = 2$ (2-exact, 0-estimate), and $n = 3$ (14-exact, 16-estimate).

What is the maximum strain of a level n structure under uniform biaxial load? In the state of maximum dilation, each unit cell is 4-fold symmetric (hence, $\varepsilon_{xx} = \varepsilon_{yy}$). The maximum dilatation states for the first 4 levels are given in Fig. 6 and their strains are shown in Table I. It is unclear whether these strains are finite as $n \to \infty$,

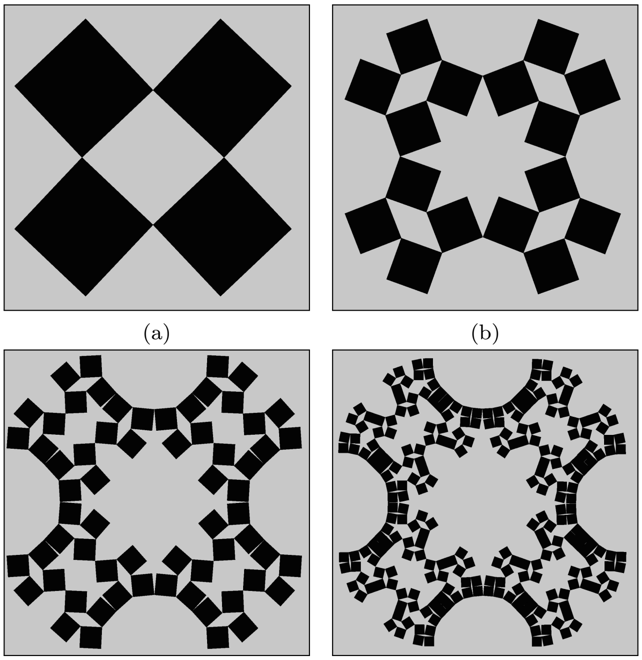

FIG. 6. States of maximum dilation of the square lattice (scaled to the same size) for $n = 1$, 2, 3, and 4 in (a)-(d), respectively.

but based on the numerical results for the first several levels we suspect that they do not.

TABLE I. Maximum dilatational strain for the square lattice for several n from analytical and numerical calculations performed using the Bullet Physics library [21].

Level n	ε^*, analytical form	ε^*, numerical value
1	$\sqrt{2}-1$	0.41
2	$\frac{7}{2\sqrt{5}}-1$	0.57
3	$\frac{1}{\sqrt{2}}-1$	0.71
4		0.82

We follow the same steps for the Kagome lattice. Level 1 may be parameterized with one angle β, as shown in Fig. 7a. To avoid self-penetration, β must satisfy $0 \leq \beta \leq 2\pi/3$. As for the square lattice, ε_{xx} and ε_{yy} are equal:

$$\begin{aligned} &\varepsilon_{xx}(\beta) = \varepsilon_{yy}(\beta) = \sqrt{3}\sin\beta + \cos\beta - 1 \\ &\varepsilon_{xy} = 0. \end{aligned} \tag{4}$$

Strains do not uniquely define the shape of a unit cell; β and $2\pi/3 - \beta$ generate the same strains, although the shapes are different (see Fig. 8). For the square lattice, replacing β with $\pi/2 - \beta$ was equivalent to rotating the unit cell by $\pi/2$, while for the Kagome lattice replacing β with $2\pi/3 - \beta$ is equivalent to rotating the unit cell by $\pi/3$.

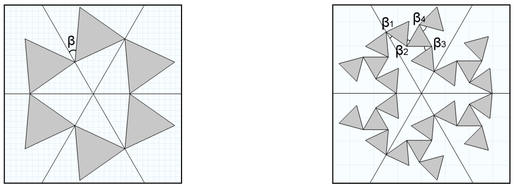

FIG. 7. Parameterization of the Kagome lattice employed here for (a) $n = 1$ and (b) 2. The solid black lines indicate mirrors.

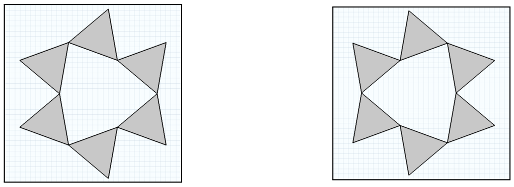

FIG. 8. Two different Kagome level 1 states that generate the same strains.

The level 1 Kagome lattice has three mirror symmetries, as shown in Fig. 7a. We employ the parameterization of the level 2 structure shown in Fig. 7b. In general, the total number of degrees of freedom for the Kagome lattice may be estimated in a manner similar to Eq. 3 ($N_{\triangle}(n) = 6 \cdot 4^{n-1}$ and $N_h(n) = 6 \cdot 4^{n-1} + 3$):

$$N_{DOF}(n) = 3N_{\triangle}(n) - 2N_h(n) = 6\left(4^{n-1} - 1\right). \tag{5}$$

As for the square lattice, this estimate is strictly valid in the limit that $n \to \infty$ since it does not remove the linearly dependent degrees of freedom. A detailed analysis of a Kagome lattice degrees of freedom was performed in [18].

Unlike for the square lattice, we were able to analytically compute the maximum dilation strain as a function of level n: $\varepsilon^* = \sqrt{3}(3/2)^{n-1} - (\sqrt{3}/2 - 1)2^{2-n} - 1$. For large n the maximum dilation strain grows exponentially with n (fully stretched states of the first three levels are shown in Fig. 2).

Making it Real(er)

Real materials, of course, are very different from the ideal free-hinge model discussed above. In this section we replace the free-hinges with spring-hinges, which is a relatively simple description of the elastic deformation that occurs in the vicinity of a hinge in a real, cut sheet. We model each hinge as a torsion spring of stiffness κ; i.e., the elastic energy of hinge i is $U_i = 2\kappa(\beta_i - \beta_i^0)^2$, where β_i and β_i^0 is the half angle between a particular pair of rigid bodies (Fig. 3a) and that angle for which the torque is zero (we omit the subscript i for level 1 structures). Unlike for free-hinges, here materials can store elastic energy and their elastic constants are, in general, non-zero. The potential energy per unit cell for the Level 1 square and Kagome lattice are $16\kappa(\beta-\beta^0)^2$ and $18\kappa(\beta-\beta^0)^2$, respectively, and for the Level 2 square is $32\kappa\left[(\beta_1-\beta_1^0)^2+(\beta_2-\beta_2^0)^2-(\beta_1-\beta_1^0)(\beta_2-\beta_2^0)\right]$.

The compliance tensor S_{ijkl} for the square lattice structures has the following form [22]:

$$\begin{pmatrix} \varepsilon_{xx} \\ \varepsilon_{yy} \\ 2\varepsilon_{xy} \end{pmatrix} = \begin{pmatrix} S_{11} & S_{12} & 0 \\ & S_{11} & 0 \\ & & S_{66} \end{pmatrix} \begin{pmatrix} \sigma_{xx} \\ \sigma_{yy} \\ \sigma_{xy} \end{pmatrix} \tag{6}$$

The number of independent elastic constants equals the number of degrees of freedom up to the point where there are more degrees of freedom than independent strain components (i.e., 3 for the square lattice and 2 for the Kagome lattice). Beyond this point, strains do not uniquely define the shape of a free-hinge unit cell. However, with hinge-springs, the strains fully define the shape of the system; the structure may be very compliant even though its primitive elements are rigid.

For the level 1 square lattice structure, there is only one degree of freedom $S_{11}=S_{12}$ and $S_{66}=0$ and for the level 2 structure there are two degrees of freedom $S_{11}\neq S_{12}$ and $S_{66}=0$. We can determine how S_{11} is related to the length of the edge of the primitive square a, the hinge stiffness κ and zero-torque half-angle β^0 for the level 1 square lattice structure. The strain ε_{xx} is related to the angle opening $\Delta\beta=\beta-\beta^0$ by

$$\varepsilon_{xx}=\frac{l-l^0}{l^0}=\frac{\cos\beta^0-\sin\beta^0}{\cos\beta^0+\sin\beta^0}\Delta\beta+\mathcal{O}(\Delta\beta^2), \tag{7}$$

such that the elastic energy per unit area is

$$U=\frac{8\kappa\Delta\beta^2}{a^2(\cos\beta^0+\sin\beta^0)^2}. \tag{8}$$

From this, we find that the elastic compliance is

$$S_{11}=a^2\frac{1-\sin 2\beta^0}{16\kappa}. \tag{9}$$

In particular, in the fully folded state $\beta^0=0$ and $S_{11}=a^2/(16\kappa)$.

The compliance tensor for hexagonal lattice structures have the following form [22]:

$$\begin{pmatrix} \varepsilon_{xx} \\ \varepsilon_{yy} \\ 2\varepsilon_{xy} \end{pmatrix} = \begin{pmatrix} S_{11} & S_{12} & 0 \\ & S_{11} & 0 \\ & & 2(S_{11}-S_{12}) \end{pmatrix} \begin{pmatrix} \sigma_{xx} \\ \sigma_{yy} \\ \sigma_{xy} \end{pmatrix} \tag{10}$$

As for the square lattice, the level 1 Kagome structure in the fully folded state ($\beta^0=0$) has only one degree of freedom; $S_{11}=S_{12}=\sqrt{3}a^2/16\kappa$ (and, of course, $S_{66}=0$), where a is a length of the edge of the primitive triangle. The level 2 (and all higher level) structure has more than two degrees of freedom and, therefore, its compliance tensor takes the general form.

For $\beta^0\neq 0$, the level 1 square and Kagome lattices retain their square and hexagonal symmetries. However, for $n>1$ this is, in general, not the case. For example, the level 2 square lattice possess square symmetry if $\beta_1^0=\pi/2-\beta_2^0$, but rectangular symmetry for $\beta_1^0\neq\pi/2-\beta_2^0$ (see Fig. 3b). Higher levels can also have oblique or rhombic symmetries.

Porous structures are often studied in the context of auxetic (negative Poisson ratio ν) materials [23]. For this class of materials, the Poisson ratio is negative for all $\beta_i^0=0$. For the level 1 lattices $\varepsilon_{xx}=\varepsilon_{yy}$, and therefore $\nu=-1$ for $\beta^0\neq\pi/4$ in the square lattice and $\beta^0\neq\pi/3$ in the Kagome lattice. When $\beta^0=\pi/4$ (square) or $\pi/3$ (Kagome), ν is not defined, since the material is fully stretched and therefore may be neither stretched nor compressed by applying uniaxial load. For $n>1$, ν is a function of the β_i^0; e.g., for a level 2 square structure $\nu=\nu(\beta_1^0,\beta_2^0)$. For a level 2 square lattice, not only is ν undefined at $(\beta_1^0,\beta_2^0)=(0,\arctan 2)$ (where the structure is fully stretched in the x-direction), but the limit does not exist as we approach this point. In fact, $\nu(\beta_1^0,\beta_2^0)$ may vary from $-\infty$ to ∞ depending on the path which is used to approach the singular point. Examination of Fig. 4 shows that the slope of the boundary $(d\varepsilon_{yy}/d\varepsilon_{xx})=\infty$ at point C, which implies $\nu=\pm\infty$ (depending on whether this point is approached from above or below). This is consistent with the numerical results in [2] where they showed that for a structure akin to our level 2, the Poisson ratio can take on large positive or negative value for a particular set of (β_1^0,β_2^0). Therefore even for level 2, the Poisson ratio may take on any value.

The results presented here suggest that it is possible to design materials with a prescribed elastic constant tensor and with **any** value of the Poisson ratio. For example, it is possible to design materials for which some elastic constants are much smaller than all of the others, for example, as described in [24, 25].

Making it Really Real

The model presented above, even with the elastic rotational hinges, involves several idealizations compared with the cut sheet. Of these, the most important are: (1) that the hinges are point hinges, when in fact the cuts leave a finite hinge ligament and (2) the assumption that the units are rigid, when in fact they are elastic bodies (see [1]). In this section, we discuss the relaxation of these two constraints by replacing the rigid blocks with isotropic elastic bodies and by making the hinges of finite size. Examples of such structures with finite hinge ligaments are shown in Fig. 9. In these examples, we employ wedge-shaped hinges of finite radius r and finite zero-torque angle, β^0. The mechanical response of such

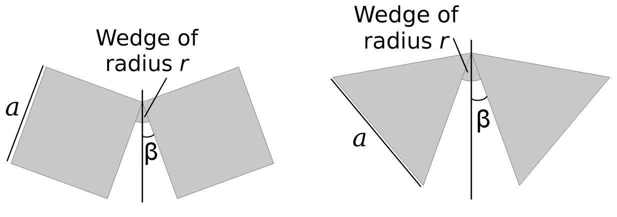

(a) (b)

FIG. 9. Wedge-shaped hinges of normalized radius, r/a, for the (a) square and (b) Kagome lattices.

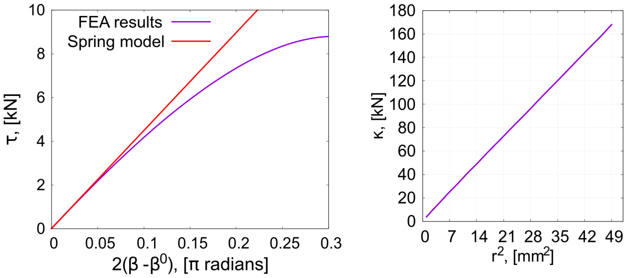

(a) (b)

FIG. 10. (a) Torque versus relative hinge angle for the geometry in Fig. 9a with hinge size $r = 2$ mm, as determined from finite element analysis and the analytical relationship for the spring hinge model. (b) The spring hinge stiffness versus hinge size as determined from FEA. For both figures $\beta^0 = \pi/18$ and $E = 2560$MPa and $\nu = 0.37$.

structures must be determined numerically.

We first investigate the relationship between the properties of a structure with such wedge-shaped hinges and the spring hinges discussed in the previous section in order to determine the applicability of the earlier results. We solve for the torque τ - rotation angle β relationship for the case where the entire material is linear elastic with elastic constants chosen for polycarbonate; i.e., the material used in our experimental work, VisiJet© SL Clear [26] (density $\rho = 1.17$g/cm^3, and isotropic linear elastic constants $E = 2560$MPa and $\nu = 0.37$). The numerical solutions are obtained using linear elastic finite element analysis (i.e., COMSOL 4.4 [27]) in plane strain (i.e., we assume the structure is infinitely thick in the direction normal to the plane of the cuts - this assumption is consistent with our experimental geometry used in the next section).

Figure 10a shows the relation between the torque per unit length and angle β for the wedge-shaped hinge in Fig. 9. The torque is a linear function of relative angle $\beta - \beta^0$, for small relative angle. However, at larger angle, the torque grows in a sub-linear manner. In the spring-hinge model, the torque is a linear function of angle: $\tau = 2\kappa(\beta - \beta^0)$. The two curves agree well (within 10%) for relative angles $2(\beta - \beta^0) < 0.12\pi = 22°$. Clearly, the spring hinge model accurately represents the real structure for small deformation. We correlate the hinge stiffness in the elastic hinge and wedge-shape hinge (finite element) models as a function of hinge size in Fig. 10b. To leading order in r, the spring hinge stiffness scales with radius as $\kappa \propto r^2$. Hinge stiffness also depends on the elastic constants of the base material. By comparison of our wedge hinge results with elastic predictions from disclination theory [28], we expect that $\kappa = \alpha E r^2$ where α is a dimensionless constant. Comparison of this relation with the finite element result in Fig. 10b, we find that $\alpha = 1.34$ for the geometry in Fig. 9a and $E = 2560$MPa and $\nu = 0.37$.

DYNAMIC ELASTIC PROPERTIES

We now examine the impact of microscopic rotational degrees of freedom on sound propagation. In particular, we exploit such rotational degrees of freedom to engineer phononic band gaps (e.g., [6]). To this end, we numerical solve the wave equation for our 2D fractal-cut materials:

$$\rho \frac{\partial^2 u_i}{\partial t^2} - \frac{\partial}{\partial x_j}(c_{ijkl}\frac{\partial u_k}{\partial x_l}) = F_i, \qquad (11)$$

where F_i is a body force, ρ is the density, u is displacement, t is time, and $c_{ijkl} = s^{-1}_{ijkl}$ are elements of the elastic stiffness tensor that depend on location (i.e., they are zero in the holes between the blocks of the base material and finite within those blocks) - theses elastic constants are not the elastic constants of the whole structure $C_{ijkl} = S^{-1}_{ijkl}$, discussed above. We look for solutions compatible with (Floquet) periodic boundary conditions: $u_i(x + ma_x, y + na_y, z) = u_i(x, y, z) \cdot \exp(-ik_x ma_x - ik_y na_y)$, where a_x and a_y are the lengths of a simulation cell in x and y directions, k_x and k_y are x and y components of wavevector $\mathbf{k}$, and m and n are integers. The numerical solutions were obtained using finite element analysis [27]. In the results presented below, we model the solid phase as an isotropic elastic body with parameters corresponding to polycarbonate [26]. We do not explicitly consider damping within the solid material or interactions between the solid material and air.

Dispersion Relations

In 2D periodic materials, the wavevectors of interest $\mathbf{k}$ are contained within the first Brillouin zone, where we use the standard notation to represent directions in reciprocal space (e.g., see [29]). The phonon band structure for the level 2 square lattice structure of Fig. 11a is shown in Figure 11b. Although results vary with level, geometrical state, and hinge size, no low frequency band gaps are observed for (level 1 and level 2) square lattices (below 50 kHz for this particular sample size).

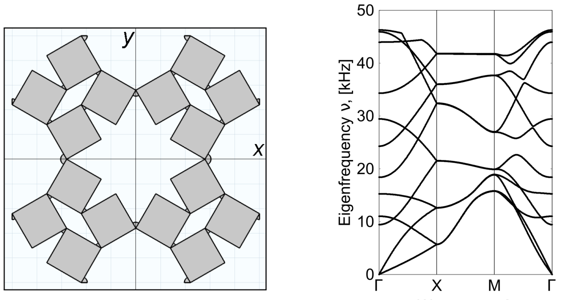

(a)

(b)

FIG. 11. The phonon band structure for the (a) level 2 square lattice structure with $(\beta_1, \beta_2) = (\pi/6, \pi/6)$ are shown in (b) for relative hinge size $r/a = 0.15$. The unit square edge length $a = 2$ mm. The solid material properties correspond to polycarbonate.

On the other hand, gaps in the phonon band structure do exist for Kagome lattices, as shown in Fig. 12 for three sets of equilibrium hinge openings for the level 2 structures shown in the insets in that figure. The general form of the band structure is independent of the opening angles (over the range of angles examined here) and, in fact, the band structure only changes slightly for the range of opening angles examined here (the magnitude of the band gap decreases slowly with increasing opening angles).

Figure 13 shows the effect of hinge size on the phonon dispersion relations. The overall form of the phonon band structure varies little with hinge size. More quantitatively, we see that the magnitude of the band gap varies by less than 5% when the hinge size r/a changes by a factor of three. On the other hand, the hinge size has a profound effect on the width of the low frequency band, although not the shapes of the individual dispersion curves within this band.

Two of the dispersion curves in Fig. 13 have non-zero slopes (sound wave group velocities) at $\mathbf{k} = \mathbf{\Gamma}$. These correspond to the long wavelength limit of the transverse and longitudinal modes [30] and are simply the static elastic stiffnesses [31]

$$\begin{aligned} C_{11} &= 4\pi^2 \rho \left(\left. \frac{d\nu_L}{d|\mathbf{k}|} \right|_{\Gamma} \right)^2 \\ C_{66} &= 4\pi^2 \rho \left(\left. \frac{d\nu_T}{d|\mathbf{k}|} \right|_{\Gamma} \right)^2 \end{aligned} \tag{12}$$

where ρ is the average density and C_{11} and C_{66} are related to the S_{ij} discussed in the static elastic properties section, above. These elastic constants (slopes) play a central role in the phonon band structure. If we scale the lower band in the band structures from Fig. 13 by their slope (or C_{11}) as $2\pi\nu/\sqrt{C_{11}/\rho}$, we find that all three band structures nearly coincide (the error in the scaling is less than 10% for a 200% change in r/a), as shown in Fig. 14. As we demonstrated above, C_{11} is proportional to the square of the hinge size r^2, so hinge size controls the location of the band gap.

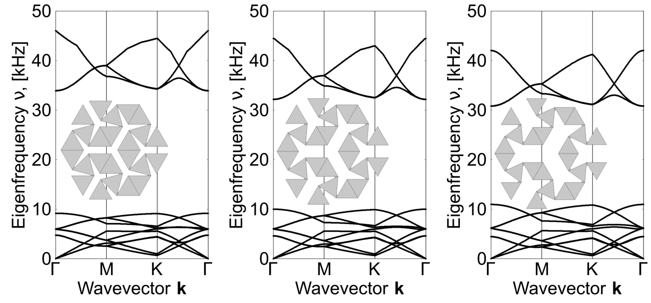

(a)

(b)

(c)

FIG. 12. Phonon band structures for level 2 Kagome lattices (see insets) for $(\beta_1,\ \beta_2,\ \beta_3,\ \beta_4)$ = (a) $(2\pi/3, \pi/12, \pi/12, \pi/12)$, (b) $(2\pi/3, 5\pi/36, 5\pi/36, 5\pi/36)$, and (c) $(2\pi/3, 7\pi/36, 7\pi/36, 7\pi/36)$ and relative hinge size $r/a = 0.15$, with unit triangle edge length $a = 2$ mm. The solid material properties correspond to polycarbonate and the β_i are as defined in Fig. 7b.

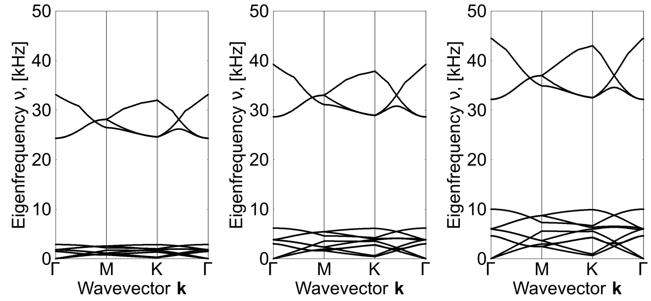

(a)

(b)

(c)

FIG. 13. Phonon band structure vs. relative hinge size for the level 2 Kagome unit cell, with $(\beta_1,\ \beta_2,\ \beta_3,\ \beta_4) = (2\pi/3,\ 5\pi/36,\ 5\pi/36,\ 5\pi/36)$ for relative hinge sizes r/a = (a) 0.05, (b) 0.10, and (c) 0.15, respectively, with unit triangle edge length $a = 2$ mm. The solid material properties correspond to polycarbonate.

Of course, as the hinge size tends to zero, the linear dispersion at small $\mathbf{k}$ goes to zero slope (no elastic restoring force), and the bands below the gap collapse (this is the free-hinge limit). The bands above the gap do not collapse in this limit. The fact that band gaps change with geometry in porous materials was noted earlier by [5] - the present results show which features of the geometry are important.

Taken together, these results demonstrate that we can independently control both the band gap and its location by separately scaling the hinge stiffness and the length scale of the overall structure (i.e., a). The band structure can be tuned further by varying the opening angles (and fractal structure level). The static elastic constants provide an accurate means of predicting the position of the bottom of the band gap.

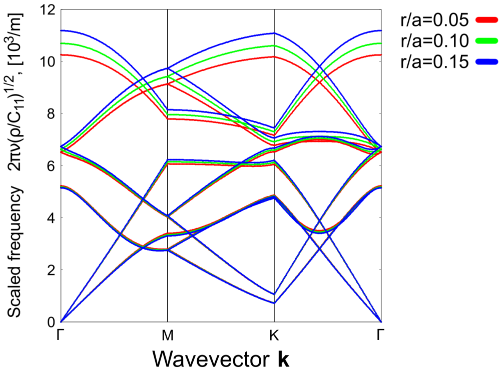

FIG. 14. Phonon band structures from Fig. 13 in which the frequency was scaled by $2\pi(\rho/C_{11})^{1/2}$.

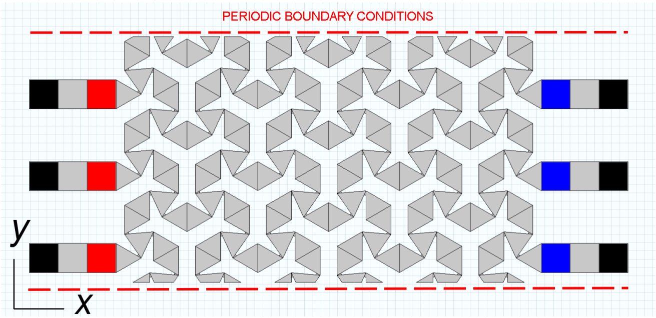

FIG. 15. Numerical model for computing transmission spectrum of a 3 unit cells thick (in the x-direction) structure. Black regions correspond to perfectly matched layers (PML), and input and output elastic energies were each integrated over the left-hand side (red) and right-hand side (blue) square blocks, respectively. A force, sinusoidally varying in time, was applied to the left edges of the red blocks.

Transmission Spectra

The phonon band structures in the previous section was determined based upon a periodic structure. On the other hand, most acoustic properties of interest are measured for finite samples. For example, one common measurement is of the acoustic transmission spectrum; the transmission coefficient T is the ratio of the output acoustic energy to the input acoustic energy through a finite thickness sample.

We examine the transmission spectrum for the level 2 Kagome lattice (periodic in y, three unit cells in x) as shown in Fig. 15. The simulations were, again, performed using the finite element package COMSOL 4.4 [27] . The sound was input into the structure through a perfectly matched layer (PML, shown in black), in order to avoid wave reflection from the boundary, via application of a harmonic force.

Figure 16 shows the transmission spectrum for the polycarbonate model in Fig. 15. This figure shows that there is substantial transmission at low frequency and again at high frequency. However, between these two frequency ranges, a large range of frequencies exist for which there is no acoustic energy transmission (i.e., a phononic band gap). Comparison of this transmission spectrum with the phonon band structure in Fig. 12b (i.e., $\beta_1 = 2\pi/3$, $\beta_2 = 5\pi/36$, $\beta_3 = 5\pi/36$, and $\beta_4 = 5\pi/36$) shows the origin of the transmission spectrum peaks and gaps.

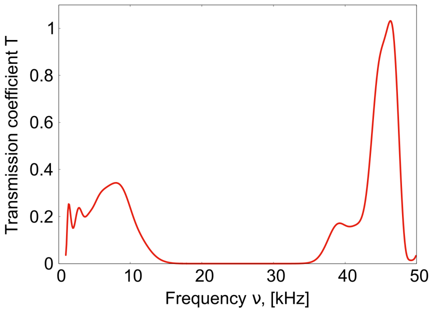

FIG. 16. Transmission spectrum for the polycarbonate model in Fig. 15. The corresponding band structure is shown in Fig. 12b.

Experimental Comparison

In order to validate the acoustic property predictions, above, we manufactured a level 2 Kagome structure, akin to that shown in Fig. 12a. The sample was produced by 3D printing (3D Systems ProJet 6000) with a polycarbonate-like material VisiJet© SL Clear [26] ($\rho = 1.17\text{g/cm}^3$, $E = 2560\text{MPa}$, $\nu = 0.37$). To reduce costs, the primitive triangular units were hollow, rather than filled (as in Fig. 12a) as seen in Fig. 17a. The entire sample was 3 unit cells thick (4.5 cm) in the x (sound propagation)-direction and 11.5 unit cells (20 cm) in the y-direction and 20 cm long in the z-direction (i.e., the sample is square in the directions perpendicular to the sound propagation direction); see Fig. 18. The calculated phonon band structure for the periodic polycarbonate sample is shown in Fig. 17b and the calculated frequency-dependent transmission coefficient for this 3 unit cell thick sample is shown in Fig. 19.

We measure the transmission spectrum of the 3D printed sample in a soundproof chamber. The sound was generated through a speaker driven by a BK Precision 4003A signal generator in a 3-25kHz frequency range. The receiving sensor, mounted on the other side of the sample from the speaker, was a Behringer ECM 8000 microphone, the output of which was amplified and recorded on a Tektronix TDS 540 oscilloscope. The transmission coefficient is the ratio between the sound intensities registered by the microphone with and without the sample. The results are compared with the numerical

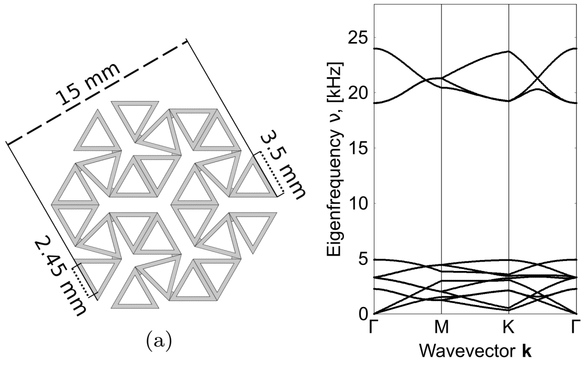

(a)

(b)

FIG. 17. The unit cell (a) and calculated phonon band structure (b) of the 3D-printed polymer structure with $r/a = 0.15$, $\beta_1 = 2\pi/3$, and $\beta_2 = \beta_3 = \beta_4 = \pi/12$.

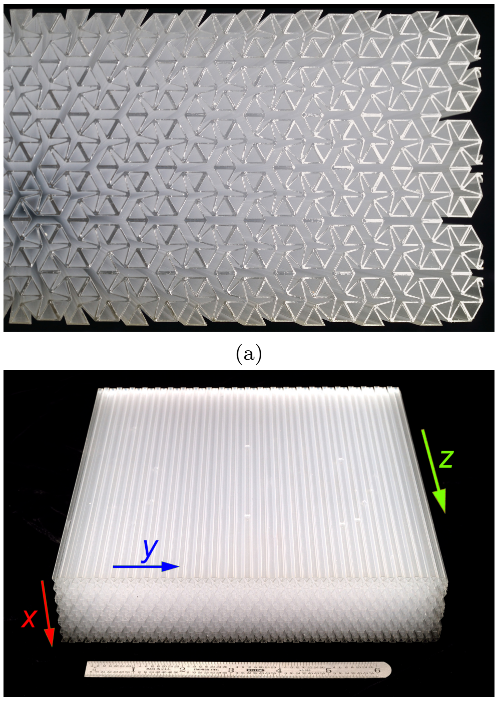

(a)

(b)

FIG. 18. 3D printed sample. In the experiment, sound propagates along the x-direction.

prediction in Fig. 19.

The finite element analysis reproduces the general form and frequency range of the experimental transmission at low frequency. Both the FEA and experiments also show the transmission coefficient going to zero below 10 kHz. However, while the FEA calculations show a pronounced peak in the transmission coefficient between 18 and 25 kHz, no such peak is observed in the experiment.

The missing high frequency peak in the transmission spectrum in the experiment may be associated with the neglect of one or more of the following factors in the FEA calculations: (1) solid-air interactions, (2) sound propagation through and dissipation in the air, (3) dissipation (damping) within the polycarbonate, and (4) out-of-plane bending (drumhead-like) modes in the sample. Of these, we expect that the neglect of damping is the most important effect at high frequency. Unfortunately, no damping data is available for our polycarbonate in the correct frequency range. High frequency damping data on a similar material is available [32] in the 2-10 MHz frequency range. This data suggests that damping grows linearly with frequency (in this range). Extrapolating this data to frequencies of interest here suggests that this damping is too small to cause significant attenuation at 22 kHz for the sample size employed here. If the material were a uniform plate, we would expect the damping associated with air to be too small to account for the present observations. However, we note that our material is extremely porous; that is, the air-polycarbonate surface area is **very** much larger than if the same mass of polycarbonate was in the form of a homogeneous plate. This large area would imply greatly enhanced damping. We suspect that this explains why the high frequency peak seen in the simulations if absent in the experimental transmission spectrum (Fig. 19).

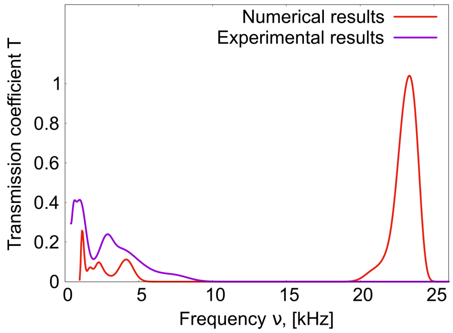

FIG. 19. The transmission spectra from the numerical model (red curve) and the experimental measurement (blue) for sample in Fig. 18.

Nonetheless, the fact that the transmission coefficient goes to zero (at a frequency similar to the predictions) is clear evidence of a phononic band gap in these materials. Unfortunately, we are unable to experimentally characterize its size. We consider this confirmation of the main theoretical predictions (albeit not strong quantitive confirmation).

CONCLUSION

In this paper, we investigated the static and dynamic elastic response of fractal-cut materials. These materials are novel in the sense that (a) they deform by rotation of “rigid” units rather than by straining these units, (b) these materials can be fabricated by exploiting a simple cutting paradigm (or fabricated by 3D printing), and (c) have both static and dynamic properties that can be manipulated by control of the cut pattern, its hierarchy (to arbitrary fractal level), and hinge size. For example, we showed that variation of fractal-cut level can be used to manipulate the symmetry of the elastic constant tensor. Our results also demonstrate how to manipulate the elastic limit of deformation (e.g., the maximum achievable dilatation before onset of macroscopic material deformation) and to design elastic response by manipulating cut structure (i.e., cut structure/elastic constant relations). We also examined phonon behavior in fractal-cut materials and showed how some cut symmetries naturally open acoustic band gaps, while others do not. We also established which features of the fractal-cut structure determine specific features of the phonon band structure. Based upon these results we predicted an acoustic transmission spectrum for a fractal-cut material and validated it via 3D printing of a structure and testing in an acoustic chamber. The results confirmed the existence of an acoustic band gap in a subset of fractal-cut materials.

ACKNOWLEDGEMENTS

The authors would like to thank Dr. In-Suk Choi for useful discussion. V.K, S.Y., Y.C., and D.J.S. acknowledge partial support from NSF/Materials Research Science and Engineering Center (MRSEC) Award to University of Pennsylvania, DMR Grant 1120901.

---

[1] Y. Cho, J.-H. Shin, A. Costa, T. A. Kim, V. Kunin, J. Li, S. Y. Lee, S. Yang, H. N. Han, I.-S. Choi, and D. J. Srolovitz, PNAS **111**, 17390 (2014).

[2] R. Gatt, L. Mizzi, J. I. Azzopardi, K. M. Azzopardi, D. Attard, A. Casha, J. Briffa, and J. N. Grima, Scientific Reports **5**, 8395 (2015).

[3] J. N. Grima and K. E. Evans, Journal Of Materials Science Letters **19**, 1563 (2000).

[4] M. Taylor, L. Francesconi, M. Gerendás, A. Shanian, C. Carson, and K. Bertoldi, Adv Mater. **26**, 2365 (2014).

[5] S. Shan, S. H. Kang, P. Wang, C. Qu, S. Shian, E. R. Chen, and K. Bertoldi, Advanced Functional Materials **24**, 4935 (2014).

[6] P. Wang, J. Shim, and K. Bertoldi, Phys. Rev. B **88**, 014304 (2013).

[7] C. W. Huang, W. Ren, V. C. Nguyen, Z. Chen, J. Wang, T. Sritharan, and L. Chen, Adv Mater. **24**, 4170 (2014).

[8] P. Langlet, A.-C. Hladky-Hennion, and J.-N. Decarpigny, J. Acoust. Soc. Am. **98**, 2792 (1995).

[9] Y.-F. Wang and Y.-S. Wang, J. Appl. Phys. **114**, 043509 (2013).

[10] L. Xiao-Jian and F. You-Hua, Chin. Phys. B **22**, 036101 (2013).

[11] N.-K. Kuo and G. Piazza, Appl. Phys. Lett. **99**, 163501 (2011).

[12] R. C. Norris, J. S. Hamel, and P. Nadeau, J. Appl. Phys. **103**, 104908 (2008).

[13] Y. Pennec, B. Djafari-Rouhani, H. Larabi, J. O. Vasseur, and A. C. Hladky-Hennion, Phys. Rev. B **68**, 104105 (2008).

[14] A. Khelif, A. Choujaa, S. Benchabane, B. Djafari-Rouhani, and V. Laude, Appl. Phys. Lett. **84**, 4400 (2004).

[15] J. Li, L. Fok, X. Yin, G. Bartal, and X. Zhang, Nature Materials **8**, 931 (2009).

[16] X. Zhang and Z. Liu, Appl. Phys. Lett. **85**, 341 (2004).

[17] Z. Liu, X. Zhang, Y. Mao, Y. Y. Zhu, Z. Yang, C. T. Chan, and P. Sheng, Science **289**, 1734 (2000).

[18] K. Sun, A. Souslov, X. Mao, and T. C. Lubensky, PNAS **109**, 12369 (2012).

[19] G. Wu, Y. Cho, I.-S. Choi, D. Ge, J. Li, H. N. Han, T. Lubensky, and S. Yang, Adv Mater. **27**, 2747 (2015).

[20] Y. Tang, G. Lin, L. Han, S. Qiu, S. Yang, and J. Yin, Adv Mater. (2015).

[21] "Bullet Physics library," `http://bulletphysics.org/` (2015).

[22] J. F. Nye, *Physical Properties of Crystals: Their Representation by Tensors and Matrices* (Oxford University Press, 1985).

[23] W. Yang, Z.-M. Li, W. Shi, B.-H. Xie, and M.-B. Yang, Journal of Materials Science **39**, 3269 (2004).

[24] G. Milton and A. Cherkaev, J. Eng. Mater. Technol **117**, 483 (1995).

[25] M. Kadic, T. Buckmann, N. Stenger, M. Thiel, and M. Wegener, "On the feasibility of pentamode mechanical metamaterials," (2012), arXiv:1203.1481.

[26] "Measuring acoustic attenuation in solids," `http://iowadoppler.com/documents/attenuation.pdf` (2015).

[27] "COMSOL Multiphysics," `http://www.comsol.com/` (2015).

[28] R. de Wit, Journal of Physics C: Solid State Physics **5**, 529 (1972).

[29] W. Setyawana and S. Curtarolo, Computational Materials Science **49**, 299 (2010).

[30] C. Kittel, *Introduction to Solid State Physics* (John Wiley & Sons, Inc., 2005).

[31] S. Haussuhl, *Physical Properties of Crystals: An Introduction* (John Wiley & Sons, Inc., 2007).

[32] "Visijet SL Clear," `http://www.3dsystems.com/es/materials/visijet-sl-clear` (2015).